Energy and Power Engineering, 2026, 18(8), 483-508
https://www.scirp.org/journal/epe
ISSN Online: 1947-3818
ISSN Print: 1949-243X

A Study on the Performance of a New-Type Swirl-Stabilized Combustor for Enhancing Boiler Low-Load Stable Combustion Capability

Hongjun Li

Production Management Department, Datang Heilongjiang Power Generation Co., Ltd., Harbin, China
Email: 365911500@qq.com

How to cite this paper: Li, H.J. (2026) A Study on the Performance of a New-Type Swirl-Stabilized Combustor for Enhancing Boiler Low-Load Stable Combustion Capability. *Energy and Power Engineering*, **18**, 483-508.
https://doi.org/10.4236/epe.2026.188023

Received: July 3, 2026
Accepted: July 31, 2026
Published: August 3, 2026

Abstract

This study experimentally investigates the gas-particle two-phase flow characteristics of an old-model burner (OMB) and a new-type swirl-stabilized combustor (NTSTC) designed for a 350 MW opposed-fired coal boiler. Using a particle dynamic anemometry (PDA) system, the three-dimensional velocity field, turbulence intensity, and particle volume flux at the burner outlet were measured at nominal load cases spanning 20% - 100%. The results show that the NTSTC forms a distinct central recirculation zone (RZ) in the near-nozzle region ($x/d = 0.1 - 0.5$), where the axial velocity exhibits a bimodal distribution and the radial velocity indicates centripetal particle movement near $r/d \approx 0.2$. These characteristics persist at low loads and promote particle residence and central accumulation. Compared with the OMB, the NTSTC exhibits higher turbulence intensity within central RZ and stronger gas-particle mixing, including 20% load. The particle volume flux results further demonstrate central particle enrichment and particle backflow within the RZ. Overall, the NTSTC provides more favorable near-field gas-particle flow organization and better aerodynamic adaptability to load variation. The present study is limited to cold-flow measurements; combustion efficiency, gas composition, and NO_x emissions were not directly evaluated.

Keywords

Swirl-Stabilized Combustor, Interstitial Air, Low-Load Combustion Stability, Gas-Particle Flow Properties, Central Recirculation Zone

1. Introduction

As China's power sector reforms deepen and its energy structure undergoes accelerated transformation, the proportion of renewable energy in primary energy consumption continues to rise. Large-scale integration of renewable energy sources into the power grid imposes stricter requirements on power system operation and control because of their intermittency and fluctuation. As the core support for peak shaving and frequency regulation in power grids, thermal power generation units play a vital role in ensuring the safe and stable operation of the power system [1]-[3], acting as the "ballast" for energy security. However, the peak regulation capacity of coal-fired units in China is currently inadequate, with the majority of units exhibiting a regulation depth of only 40% - 50% [4] [5], thereby complicating the fulfilment of flexibility demands in the context of high renewable energy integration. In response, the National Energy Administration released the Implementation Plan for the Special Action on Optimizing Power System Regulation Capabilities (2025-2027) in 2025. The plan stipulates that by 2027, all existing coal-fired units must undergo retrofitting to enhance their flexibility, in accordance with the principle of "retrofitting all coal-fired units that are eligible for upgrading". Additionally, it explores avenues for implementing deep flexible peak regulation while ensuring safety [6] [7]. This means that specific coal-fired units must operate stably at 30% or even 20% of rated capacity while meeting low-emission requirements [8], to meet future power system demands for deep peak regulation and frequent start-stop operations.

From the standpoint of fuel makeup, China's coal endowment includes sizable shares of lean coal and anthracite—about 5.5% and 11.5% of proven reserves, respectively—and these fuels account for over 40% of what coal-fired plants actually burn, making them pivotal in the national energy mix [9] [10]. Bituminous coal with ash content above 40% or a lower heating value below 16.7 MJ/kg is designated low-grade bituminous coal; anthracite and lean coal are likewise categorized as low-quality coals [11]. Such fuels typically suffer from difficult ignition, incomplete burnout, and low combustion efficiency, and at low loads they are especially susceptible to instability or even flameout. Currently, units firing low-quality coal generally sustain a minimum stable load of only ~45%, which falls short of the 20% - 30% low-load, steady-combustion targets under high renewable integration. Therefore, improving the low-load stability and deep peak-shaving flexibility of boilers using low-quality coals has become a pressing technical priority.

Under low-load operation conditions of the boiler, a significant reduction in furnace temperature occurs, which adversely affects the ignition and combustion processes of pulverized coal, thereby greatly increasing the likelihood of flameout [12]. Traditional approaches mainly rely on micro-oil or plasma-assisted combustion to maintain flame stability. However, these ignition assistance techniques face challenges such as burner damage, extensive wear of oil and plasma equipment, and poor economic performance. Furthermore, when low-quality coal is blended in high proportions, the flame stabilization effect is limited, and the coal's adaptability is inadequate. In contrast to ignition assistance methods, self-stabilizing combustion technology improves the flow field and flame stability through the optimization of burner design, thus providing better safety and cost-effectiveness. The fundamental principle of this technology is to effectively direct and regulate the recirculation zone (RZ) at the burner outlet. This RZ extends the residence time of particles and boosts energy and mass transfer with high-temperature flue gas, thereby enhancing ignition conditions and combustion efficiency. Especially under 20% - 30% rated load and with lean coal combustion, the optimized RZ significantly improves flame stability and reduces pollution during combustion.

In recent years, numerous researchers have achieved significant results in optimizing RZ design by improving burner structures. For instance, Yuan *et al.* [13] proposed a novel swirl combustor with a radial staged air supply. The results of the cold-state gas-solid two-phase flow modeling experiment indicate that under both single-layer and double-layer radial staged air configurations, parameters such as the three-dimensional mean velocity reveal a large central RZ in the furnace. The double-layer configuration was found to impede gas-solid mixing, thereby further reducing NO_x emissions and mitigating particle erosion on water-cooled walls to a certain extent. Zhao *et al.* [14] developed a petal-shaped swirl combustor. Numerical simulation results indicate that this combustor forms a distinct RZ behind its petal structure, thereby improving pulverized coal ignition conditions and flame stability. The industrial testing of a 210 MW unit burning coal with V_{daf} = 12% - 18% further validated its combustion stability performance, achieving a minimum stable load (MSL) as low as 55%. Yan *et al.* [15] investigated a novel swirl combustor through laboratory testing and industrial application. Their findings revealed that internal secondary air plays a critical role in combustion characteristics and emission performance. By enhancing the mixing of fuel and air, this combustor attained low NO_x emissions (364.9 mg/m^3) and exhibited remarkable engineering adaptability without experiencing slagging issues during extended operation. Su *et al.* [16] combined numerical simulations with industrial tests to propose an optimization of the internal secondary air cone structure of low-NO_x swirl combustors, thereby effectively enhancing aerodynamic characteristics and combustion performance. The study demonstrated that an expanded cone design enhances the entrainment of primary and secondary air, forming a stable RZ that significantly improves combustion stability under low-load operating conditions. Experimental results closely matched numerical predictions, validating the feasibility of this optimization scheme. Through numerical simulations and full-scale tests, Song *et al.* [17] demonstrated that incorporating a blunt body into a reverse-jet swirl pulverized-coal burner improves recirculation and flame stability. The findings indicated that this measure led to a substantial reduction in fly ash carbon content, from 18.63% to 8.55%, and a notable decrease in NO concentration, by approximately 8%. These observations suggest a considerable impact on enhancing combustion efficiency and reducing emissions.

In summary, existing research has made some progress in optimizing the RZ through burner structural improvements, but significant limitations remain. From a design trend perspective, most burners tend to adopt complex structures such as guide vanes, blunt bodies, and staged air channels to enhance the recirculation effect. While these approaches have partially improved low-NO*x* combustion and mitigated slagging, they have failed to integrate stable combustion enhancement with structural simplification. Instead, they have led to increased structural complexity, maintenance difficulties, and manufacturing costs. Furthermore, existing evaluation systems primarily focus on combustion stability under medium-to-high load conditions, with experimental objectives centered on achieving low NO*x* emissions and preventing slagging. However, against the backdrop of large-scale grid integration of new energy sources and the requirement for thermal power units to undertake deep flexible peak regulation tasks, the aforementioned research directions exhibit limitations. Under low-load conditions, the air and coal feed rates for middle and lower burners must be significantly reduced, with some burners remaining inactive for extended periods. This causes significant deviations in the furnace temperature field and fuel concentration distribution from design conditions. Under these circumstances, focusing solely on combustion stability at medium-to-high loads no longer meets operational requirements. Therefore, future burner design and low-load stable combustion research must be closely aligned with deep peak regulation requirements. The focus should shift to exploring novel structures and operational mechanisms that maintain flame stability and achieve low pollutant emissions at 20% - 30% of rated load or even lower. Only by incorporating low-load performance into the core objectives of burner optimization can we effectively support the flexibility retrofitting and clean, efficient operation of coal-fired power units.

In order to address the issue of insufficient combustion stability during low-load operation in a 350 MW opposed-fired coal boiler burning lean coal, this paper proposes the adoption of a NTSTC to enhance its combustion performance under low-load conditions. The airflow structure at the burner outlet and the movement characteristics of pulverized coal are key factors in evaluating combustion stability. Accordingly, a gas-solid two-phase flow experimental platform was established to measure the three-dimensional velocity field at the burner outlet under 20% - 100% of the rated load, and to analyze the distribution patterns of turbulence intensity and particle volumetric flow rate. The combustion characteristics of NTSTC and OMB burners at different loads were systematically evaluated through experimental methods. The primary objective of this study was to investigate the mechanism by which NTSTC enhances boiler combustion efficiency, stability, and low-load adaptability. Experimental results revealed an intrinsic coupling relationship between burner design and combustion processes, thereby providing a scientific basis for optimizing boiler performance and ensuring stable operation. Through systematic experimental comparison and in-depth analysis of the two types of swirl combustors, this study not only expands the existing understanding of burner flow and combustion behavior but also deepens insight into the stabilization mechanism of swirl combustors. The research outcomes provide valuable theoretical and experimental support for the broader application of swirl combustor technology, as well as meaningful references for the future optimization and retrofitting of coal-fired boiler burners and deep peak-shaving operations.

2. New-Type Swirl-Stabilized Combustor

The structure of OMB is shown in Figure 1. The OMB employs a concentric multi-air-channel configuration to achieve staged air supply and swirl-stabilized combustion. The burner primarily consists of the following components: ignition device (1), swirl channel (2), internal secondary air inlet (3) connected to the internal secondary air channel (4), and internal secondary air guide vanes (5). The secondary air system further comprises tertiary air guide vanes (6), external secondary air guide vanes (7), and their corresponding channels (8 - 9). The inner secondary air guide vanes are axially arranged and adjustable to control axial momentum and swirl intensity. In contrast, the outer secondary air guide vanes are tangentially arranged with adjustable angles to generate strong circumferential velocities. The tertiary air and central air guide vanes feature fixed axial structures, providing a stable axial flow field.

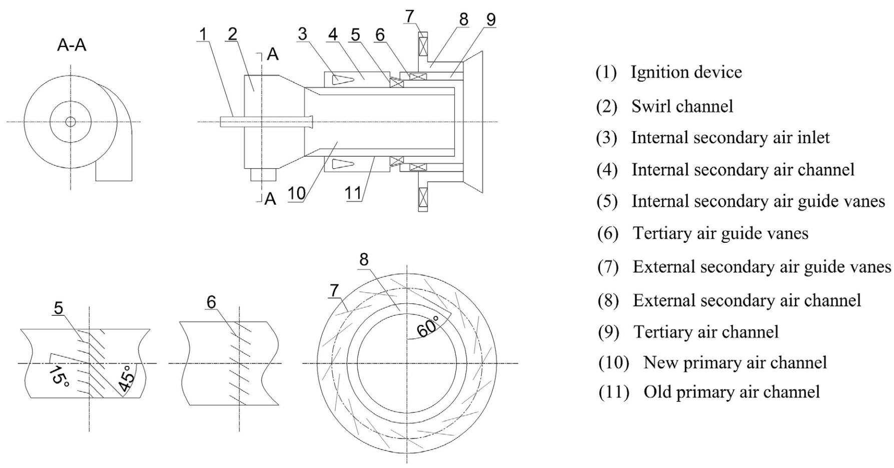

Figure 1. The structure of OMB.

The burner's structural parameters are listed in Table 1. For the OMB, the cross-sectional area of the primary-air channel accounts for 32.6% of the total burner outlet area. For the NTSTC, the corresponding proportion is 29.7% because of the additional interstitial-air channel. In practical applications, this burner fails to maintain stable operation of the pulverized coal boiler at 20% of rated load. Field investigations and previous studies show that the coal-feed elbow alone cannot provide sufficient swirl (tangential momentum) to the primary air–coal mixture. Moreover, pulverized coal is injected in a highly dispersed manner, which undermines combustion under low-load conditions. In addition, the inner secondary air guide vane is located relatively far from the primary air outlet; the swirl associated with the inner secondary air therefore hinders establishment of a stable RZ in the burner outlet region, which is another critical contributor to low-load combustion instability.

Table 1. Structural parameters of OMB and NTSTC.

Nozzle area/m^2	NTSTC	OMB
Central air	/	/
Primary air	0.2771	0.2771
Interstitial air	0.0822	/
Internal secondary air	0.2270	0.2270
Tertiary air	0.1073	0.1073
External secondary air	0.2391	0.2391

To address the poor combustion stability of the OMB during low-load operation, this paper proposes a NTSTC. The structure of the NTSTC is shown in **Figure 2**. The structural parameters of the combustor are listed in **Table 1**. Unlike the OMB, the NTSTC primarily consists of the following components: a novel primary air channel (1), an interstitial air control valve (2), an interstitial air channel (3) equipped with interstitial air axial guide vanes (4), a three-stage fuel enrichment ring (5) for central coal concentration, an interstitial air diffuser (7), and an inner secondary air diffuser (6). The remaining components are consistent with the OMB.

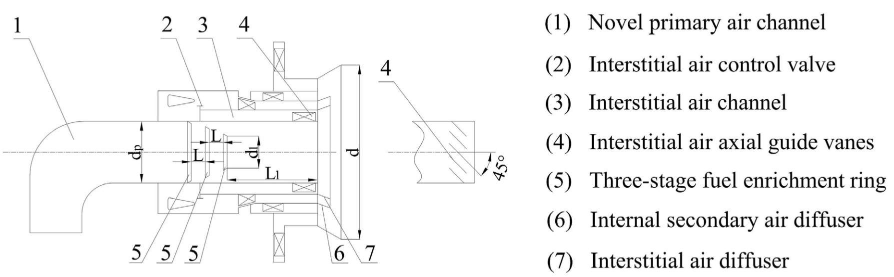

Figure 2. The structure of NTSTC.

Based on the OMB design, the ignition device and swirl device in the primary air channel were removed. A new primary air channel with a coal-feed elbow was adopted, while the nozzle area remained unchanged. Secondly, three-stage fuel enrichment rings were added to the primary air channel in the NTSTC to enhance the radial enrichment effect of pulverized coal. The inner diameter of the primary air channel is defined as d_p. The spacing between each stage of the enrichment rings is L ($L = 0.2d_p$). The diameter of the third-stage enrichment ring is d_1 ($d_1 = 0.5d_p$). The distance from the third-stage enrichment ring to the primary air nozzle is L_1 ($L_1 = d_p$). In this design, the addition of a fuel enrichment ring effectively increases the pulverized coal concentration in the central region of the air channel, bringing several significant advantages. The enhanced coal concentration in the central zone prolongs the particle residence time in the RZ. This allows for more thorough contact between the coal powder and high-temperature flue gas, thereby absorbing more heat and achieving a better preheating effect. This improved preheating raises the combustion temperature of the coal powder, further promoting its complete combustion and enhancing combustion efficiency. Meanwhile, an increase in pulverized coal concentration reduces the ignition heat required during startup. The elevated fuel quantity per unit volume facilitates easier and faster ignition of the pulverized coal, thereby shortening the ignition time and ensuring rapid flame establishment. This enhancement significantly improves combustion stability and prevents unstable combustion phenomena caused by ignition delay. Through this optimized design, not only is the preheating efficiency of the pulverized coal improved, but the ignition characteristics are also enhanced, ensuring an efficient and stable combustion process. Furthermore, an interstitial air channel is introduced between the new and existing primary air channels, equipped with corresponding guide vanes to effectively regulate airflow distribution and promote momentum exchange. The interstitial air guide vanes are precisely positioned adjacent to the primary air nozzle, designed to impart sufficient swirl momentum to the interstitial air before it enters the burner nozzle region. This configuration promotes the formation of a distinct RZ near the nozzle, enabling effective heating of the coal particles by the reflux of high-temperature flue gas. The primary function of the interstitial air nozzle and the inner secondary air inlet with an expanded structure is to enhance airflow stability and uniformity by reducing airflow velocity and improving its distribution. The expansion allows for a smoother entry of air into the burner, reducing localized disturbances caused by uneven or excessive air speed. This helps prevent unstable airflow distribution while promoting uniform preheating of coal particles in the nozzle region. Furthermore, the expanded structure facilitates the formation of a well-developed RZ, enabling high-temperature flue gas to effectively recirculate and heat the coal particles, thereby improving combustion efficiency and stability. This design optimizes both the airflow and coal particle distribution within the burner, ultimately enhancing the overall stability and efficiency of the combustion process.

NTSTC offers the following key advantages:

1) low-load stable combustion

In terms of swirl combustion stabilization mechanisms, Ti *et al.* [18] highlighted that the presence of a high-temperature, oxygen-deficient RZ at the burner outlet is crucial for achieving stable combustion. The structural improvements implemented in this study, through the synergistic effect of the primary air channel and the three-stage enrichment ring, create a region with a high concentration of coal particles, elevated temperature, and appropriate oxygen levels in the center of the burner outlet. This environment provides favorable conditions for stable combustion of the coal powder. The high concentration of pulverized coal ignites more readily under the influence of high-temperature flue gas carried by the recirculation flow. This improvement in the early ignition conditions of the combustion system effectively reduces ignition delay time. Additionally, the newly introduced swirling gap air generates the necessary rotational momentum through guide vanes in the gap, inducing the primary air to swirl and enhancing the shear and mixing effect with the secondary air. This not only enhances the oxygen supply to the combustion zone but also facilitates rapid coupling between the fuel-rich and oxygen-rich air streams, thereby optimizing combustion efficiency and stability. Numerous studies have indicated that the outlet RZ plays a pivotal role in enhancing boiler combustion stability and adapting to varying operating conditions [19]-[21].

2) NTSTC and OMB have the same secondary air resistance

In the design of the NTSTC, the layout of the inner secondary air, outer secondary air, and tertiary air channels along with their guide vanes was adopted from the OMB burner, ensuring that the velocity field and swirl characteristics of the secondary air remained unchanged. Consequently, the NTSTC maintains consistent secondary airflow resistance with the prototype burner. After the retrofitting of this technology on a selection of boiler burners, the secondary air velocity distribution between the new and old burners has been found to remain consistent. This ensures the coordinated and stable operation of both types within the furnace, thereby preventing the generation of deleterious flow disturbance effects.

3) Low NO_x emissions and slagging prevention

Studies have demonstrated that the high-temperature, low-oxygen reducing environment in the RZ at the outlet of swirl burners can significantly reduce the formation of fuel NO_x [22] [23]. Within the NTSTC, pulverized coal is highly concentrated in the central outlet region. The particles demonstrate a substantial volume fraction and protracted residence time within the RZ, which further intensifies the local reducing conditions. Within this enrichment zone, the combustion process of pulverized coal is dominated by reducing conditions, which effectively reduces pathways for fuel NO_x formation and enhances overall emission reduction efficiency. In the NTSTC, after being progressively concentrated by three-stage fuel enrichment rings, pulverized coal is injected through the central primary air channel. The tangential and radial velocity components of the fuel jet are relatively negligible. This ejection characteristic serves to concentrate the majority of the pulverized coal in the burner's central region following its exit from the outlet, thereby forming a distinct enrichment zone. This design effectively mitigates the propensity of pulverized coal to migrate toward furnace walls, thereby significantly reducing the risk of slagging and ash accumulation.

3. Methodology

The prototype boiler was a 350 MW supercritical opposed-fired pulverized-coal boiler, model HG-1146/25.41-PM1, equipped with 20 swirl burners arranged in five elevations on the front and rear walls. The boiler was operated with blends of Yangquan lean coal and Caojiahuochang bituminous coal. The Yangquan lean coal had M_{ad} = 0.60%, V_{ad} = 8.45%, A_{ad} = 19.30%, FC_{ad} = 71.65%, and $Q_{net,ar}$ = 27.12

MJ/kg. Under the full-load design condition, the primary-air and secondary-air temperatures were 94˚C and 313˚C, respectively. The primary-air and total secondary-air mass flow rates of each prototype burner were 5.46 kg/s and 11.79 kg/s, respectively. The airflow rates of the 1:7 cold model were derived from the plant operating records while preserving geometric similarity, operation within the second self-similar Reynolds-number regime, and the momentum ratios among the air streams. All cold-model tests were conducted with the primary air and secondary air at 15˚C. For the OMB, the nominal 100%, 50%, 40%, and 20% cold-model cases represented the air-distribution schemes used at plant loads of 60% - 100%, 47% - 50%, 30% - 40%, and approximately 20%, respectively. For the NTSTC, the nominal 100%, 40%, and 20% cold-model cases represented the air-distribution schemes applicable to plant loads of 50% - 100%, 30% - 40%, and approximately 20%, respectively.

3.1. Cold-Model Gas-Particle Flow Experiment System

Gas-particle two-phase flow is universally present in processes such as pulverized coal combustion, pneumatic conveying, and dust removal, exhibiting highly complex turbulence structures. In coal-fired utility boilers, the mixed flow of pulverized coal and air represents a typical gas-particle two-phase flow phenomenon. Rational organization of the coupling process between coal particles and the air stream is a crucial prerequisite for achieving stable combustion in the furnace, high burnout efficiency, and low NO_x emissions. However, due to limitations in field conditions, it is difficult to obtain the flow field characteristics of the burner under actual operating conditions. Therefore, most scholars employ cold gas-particle two-phase flow scaling experiments to study the flow characteristics of scaled-down burners. Previous research indicates that the velocity and particle concentration distributions in actual reactive flows are similar to those obtained from cold gas-particle two-phase experiments. Consequently, provided that similarity criteria are satisfied, results from cold-flow experiments can accurately reflect the actual gas-particle flow characteristics in the burner outlet region [24]-[26]. Thus, this study utilizes a three-dimensional Phase Doppler Anemometer (PDA) to measure the gas-particle flow characteristics in the burner outlet region, focusing on revealing the influence of primary air velocity variations on the gas-particle flow characteristics in the outlet regions of the OMB and NTSTC burners.

In terms of experimental design and parameter calculation, this study adheres to the following similarity criteria [13] [27]. Generally, it is very difficult to satisfy all these criteria completely; the usual approach is to neglect some non-deterministic criteria and perform approximate scaling:

1) Geometric similarity between model and prototype: The geometric scale ratio between the model and the prototype is 1:7.

2) Flow in the second self-modeling zone: The Reynolds numbers of the model and the prototype are equal, or the Reynolds number of the model is within the second self-modeling zone. The Reynolds numbers of all nozzle airflows in this

experiment are greater than 10,800, allowing the flow to be considered within the second self-modeling zone.

3) Equal momentum ratio: The momentum ratios between the primary air-coal particle flow and other air streams in the model are equal to the corresponding ratios in the actual prototype operation.

4) Froude criterion: For most forced flows, the Froude number is not very important compared to other dimensionless numbers, such as the Reynolds number. In the scaling process of inertial separation equipment, if the particle size is below 200 μm, the influence of the Froude number can be neglected. In this experiment, the density of the glass microspheres used is 2500 kg/m^3, which is much greater than the gas density; thus, the effect of buoyancy on the particles is far less than that of gravity. Furthermore, all particle sizes used in this experiment are much smaller than 200 μm, allowing the Froude number to be neglected.

5) Gas-particle two-phase slip similarity: To ensure that the velocity "slip" in the gas-particle two-phase flow of the model is consistent with the prototype, the velocity of the pulverized coal particles in the primary air is set to 0.8 times the primary air velocity. Further details on similarity criteria can be found in Reference [28].

The purpose of the present cold-model experiment is to compare the intrinsic near-field gas-particle flow characteristics of the OMB and NTSTC, rather than to reproduce the entire furnace flow field. In the near-burner region investigated in this study, the velocity field, RZ formation, turbulence intensity, and particle volumetric flux are governed primarily by the burner geometry and the momentum distribution among the individual air streams. In the prototype opposed-fired boiler, the spacing between adjacent burners allows each burner jet to develop initially as an individual flow before substantial jet interaction occurs farther downstream. Therefore, a single-burner model is considered sufficient for identifying the effects of burner structure and air distribution on the outlet flow characteristics and for providing a consistent comparison between the OMB and NTSTC. Nevertheless, interactions with neighboring burners, the opposing-wall jets, the furnace walls, and the furnace-scale recirculating flow may alter the jet trajectory, RZ size, particle dispersion, and mixing behavior farther downstream. Consequently, the present results should be interpreted as representing the intrinsic near-field characteristics of an individual burner, while their applicability to full-furnace combustion performance requires furnace-scale verification. The cold gas-particle two-phase flow scaling experimental facilities and the arrangement of measurement points are shown in **Figure 3**.

The two-phase experimental system consists of an induced draft fan, a cyclone separator, a PDA measurement system, a screw feeder, a model burner, a scaled furnace, and connecting ducts. A negative pressure is created within the scaled furnace by the induced draft fan to drive the gas circulation, drawing air from various wind ducts into the furnace. The experimental airflow channels include primary air, gap air, inner secondary air, and outer secondary air. The air mass

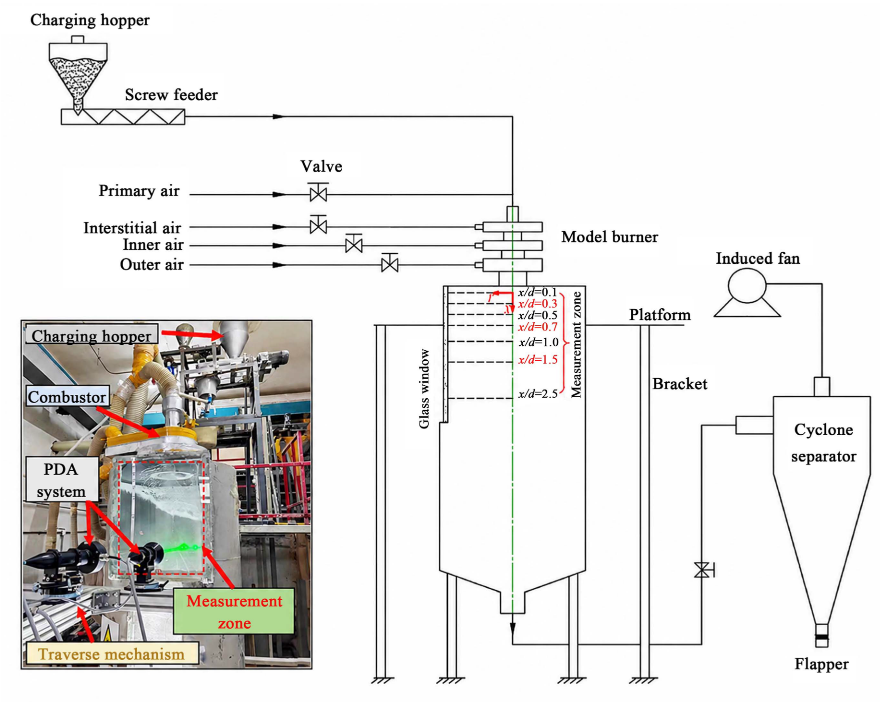

Figure 3. Experimental facilities and measurement points arrangement.

flow rate is controlled by adjusting the opening of ball valves. U-tube manometers are installed on each air supply duct, and the actual airflow rate within the duct is obtained by converting the manometer readings. To simulate the gas-particle two-phase flow in the experiment, glass microspheres are fed from an upper hopper into a screw feeding device and then uniformly conveyed into the primary air duct. After fully mixing with the carrier gas, they enter the model burner, forming an air-powder mixed airflow equivalent to the actual pulverized coal flow. After the gas-particle mixture passes through the model furnace, the particles are separated from the gas stream in a cyclone separator installed at the bottom. The collected glass microspheres can be recycled, ensuring the repeatability of experimental conditions and the reliability of the measurement results. To obtain flow field information within the furnace, multiple measurement sections are arranged downstream of the burner outlet. The measurement positions are expressed using the dimensionless distance x/d, where d is the nozzle diameter of the outer secondary air duct (d = 0.201 m). A total of seven measurement sections are set along the central axis of the burner, at positions x/d = 0.1, 0.3, 0.5, 0.7, 1.0, 1.5, and 2.5. The radial coordinate is denoted by r, defined as the radial distance from the measurement point to the nozzle centerline. Considering the large gradients in gas-particle flow velocity and particle concentration near the nozzle, the measurement points in this region are arranged more densely to capture the detailed flow characteristics under intense turbulent mixing. In regions farther from the nozzle, where the flow gradually stabilizes, the spacing between measurement points is appropriately increased to reduce redundant measurements. To avoid interference from the nozzle edge on laser measurements, the first measurement section is set at x/d = 0.1. This ensures the representativeness of the starting measurement point and allows for the acquisition of key data in the initial development stage immediately after the nozzle outlet.

The experiment employed PDA to measure the particle velocity, size, and volumetric distribution within the furnace. Its measurement ranges and accuracies are listed in **Table 2**: the velocity range is −500 to 500 $m \cdot s^{-1}$ with an accuracy of 1%; the particle size range is 0.5 to 1000 μm with an accuracy of 4%; the particle concentration range is 0 to 10^6 particles·m^{-3} with an accuracy of approximately 30%. The experimental uncertainty primarily stems from airflow fluctuations induced by the draft fan, approximately 5%, caused by variations in voltage, ambient pressure, and temperature, yet it has a minor impact on the overall results. At each measurement point, the PDA measurements were independently repeated three times under the same operating condition. For each run, data were acquired for at least 60 s, and the measurement was continued until no fewer than 5000 validated particle signals had been recorded. The three-dimensional mean velocities, root-mean-square fluctuating velocities, turbulence intensity, and particle volumetric flux were calculated separately for each run and then averaged over the three runs. The gas-phase and particle-phase swirl numbers, S_g and S_p, were calculated independently for each run using the velocity and particle-flux data measured at the x/d = 0.1 section, and the reported values represent the averages of the three runs. Repeatability was evaluated using the relative standard deviation of the repeated measurements. The maximum relative standard deviations did not exceed 5% for the mean velocities, 8% for the turbulence intensity, 10% for the particle volumetric flux, and 6% for both S_g and S_p. These results indicate that the PDA measurements and the derived parameters exhibited satisfactory repeatability. It is noteworthy that since PDA can only measure the flow of particles, it is necessary to utilize particle-phase particles to track the gas phase. According to the scaling criteria, the Stokes number (St) reflects the influence of inertial forces on the flow. When St is much less than 1, the inertial forces of the particles are negligible, allowing the particles to effectively track the gas phase. The calculation formula for St is [29]:

$$St = \frac{\rho_p d_p^2 V_1}{18 \mu_g D_1} \tag{1}$$

where: In the formula, ρ_p and d_p are the density and particle size of the particle-phase particles, in kg/m^3 and m, respectively; u_g is the dynamic viscosity of the gas phase, in $kg/(m^{-1} \cdot s^{-1})$; D_1 and V_1 are the inner diameter of the primary air nozzle and the primary air velocity, in m and m/s, respectively.

Considering variations in the primary air velocity, the maximum value corresponding to the primary air velocity was selected for calculation. The Stokes numbers for the model burner are shown in **Table 3**. It can be observed that when the glass microsphere particle size is ≤10 μm, the maximum St value for the burner is

Table 2. Measurement range and accuracy of PDA.

Parameter	Velocity ($m\cdot s^{-1}$)	Particle diameter (μm)	Particle concentration (particles·m^{-3})
Measurement range	−500 - 500	0.5 - 1000	0 - 10^6
Measurement precision	1%	4%	30%

≤0.110, indicating that the glass microspheres exhibit good tracking characteristics with the air and can serve as tracer particles for the gas phase. When the glass microsphere particle size is >10 μm, the minimum *St* value for the burner is 0.435, indicating that the glass microspheres are significantly influenced by inertial forces. Therefore, this experiment uses glass microspheres with a particle size of less than 10 μm as gas-phase tracer particles, and glass microspheres with a particle size of 10 - 100 μm as particle-phase tracer particles.

Table 3. *St* value of the model burner.

Particle diameter	*St* value
2	0.003
5	0.029
8	0.068
10	0.110
20	0.435
30	0.975
40	1.734
50	2.714
60	3.904
70	5.314
80	6.941
90	8.875
100	10.845

The gas-phase and particle-phase RZ boundaries were determined independently from their respective axial average velocity distributions. At each axial measurement section, the region with a negative axial average velocity was identified as an RZ. Each radial RZ boundary point was defined as the zero crossing of the corresponding axial average velocity profile. When the zero crossing was located between two adjacent measurement points, its radial position was determined by linear interpolation between the two points with axial average velocities of opposite signs. The boundary points obtained at successive axial sections were then connected to form the upper and lower RZ boundaries. This procedure was applied separately to the gas-phase and particle-phase data, and no interpolated combined gas-particle velocity field was constructed. The RZ length and width reported in this study were determined from the gas-phase RZ boundary, whereas the particle-phase RZ boundary was presented separately to characterize the spatial range of particle recirculation.

3.2. Test Conditions and Parameters

In this study, to quantitatively characterize the rotational characteristics of the gas-particle two-phase flow, the calculation of the swirl number (S) was introduced. As an important dimensionless parameter describing the rotational intensity of the flow field, the swirl number is widely used in the study of burner flow characteristics. Its magnitude directly relates to the flow stability, combustion efficiency, and pollutant emission characteristics within the furnace. The gas-phase swirl number S_g (Equation (2)) is calculated based on the velocity distribution and angular momentum of the airflow, reflecting the variation pattern of the gas rotational intensity downstream of the burner nozzle. The particle-phase swirl number S_p (Equation (3)) is solved considering the inertia of pulverized coal particles and the forces exerted by the airflow, revealing the rotational response of coal particles under gas-particle coupling effects. The determination of both two-phase swirl numbers is based on synchronously measured experimental data in the near-field region of the nozzle (this study selects the $x/d = 0.1$ cross-section), ensuring that the calculated results representatively reflect the initial flow characteristics at the nozzle.

Through a comparative analysis of the gas-phase and particle-phase swirl numbers of the burner under different rated loads, the coupling characteristics of the gas and particle phases inside the burner and their impact on combustion performance can be more clearly revealed. This method not only provides a quantitative basis for understanding the inherent laws of gas-particle flow at the burner outlet but also lays a theoretical foundation for the subsequent formulation of combustion optimization and emission reduction strategies.

$$S_g = \frac{\int_0^{d/2} \rho_g u_g \omega_g r^2 \mathrm{d}r}{d\int_0^{d/2} \rho_g u_g^2 r \mathrm{d}r} \tag{2}$$

$$S_p = \frac{\int_0^{d/2} \rho_p \omega_p \dot{Q} r^2 \mathrm{d}r}{d\int_0^{d/2} \rho_p u_p \dot{Q} r \mathrm{d}r} \tag{3}$$

where: ρ_g is the density of gas phase, kg/m^3; ρ_p is the density of particle phase, kg/m^3; u_g is the axial velocity of gas phase, m/s; u_p is the axial velocity of particle phase, m/s; ω_g is the tangential velocity of gas phase, m/s; ω_p is the tangential velocity of particle phase, m/s; $\dot{Q}$ is the particle volume flow at the measuring point, m^3/(m^2·s).

The test conditions and relevant parameters for the gas-particle two-phase flow scaling experiment are listed in **Table 4**. For the OMB burner, the air distribution scheme determined at 100% rated load is applicable not only to full-load operation but also stably covers operations down to 60% load. The air distribution method adopted at 50% rated load primarily targets low-load operation within the 47% - 50% range. In contrast, the NTSTC burner incorporates a gap air channel in its structure, enabling the air distribution at 100% rated load to be flexibly adapted to a wider range of operating conditions, specifically from 50% to 100% rated load, demonstrating better operational adaptability. In the actual operation of utility boilers, combustion organization at low loads is often the most complex and sensitive. Based on unit operational experience and results from multiple preliminary cold-state tests, this study determined the air distribution strategy suitable for deep peak shaving: when the unit operates within the 30% - 40% rated load range, the air distribution pattern for 40% rated load is adopted; during operation at 20% rated load, the 20% rated load air distribution is selected as the baseline condition. It must be emphasized that the OMB burner often suffers from insufficient combustion stability and severe nozzle slagging issues at low loads, adversely affecting the unit's flexible peak shaving capability.

The load cases were not identical for the two burners because their applicable air-distribution ranges were different. A separate 50% case was retained for the OMB because its 50% air-distribution scheme was specifically required for operation within the 47% - 50% load range. In contrast, the 100% air-distribution scheme of the NTSTC was applicable over the wider 50% - 100% load range; therefore, an additional 50% NTSTC case would have represented the same air-distribution scheme and was not included. Direct OMB-versus-NTSTC comparisons were conducted only at the common nominal loads of 100%, 40%, and 20%. At each common load, the primary-air flow rate and the secondary-air flow rate excluding interstitial air were identical for the two burners. The additional interstitial-air stream was retained only for the NTSTC because it is an inherent component of its structural design. Therefore, the comparison isolates the influence of the interstitial-air channel and the associated structural modification under equivalent load and baseline airflow conditions.

The experimental matrix included OMB cases at 100%, 50%, 40%, and 20% rated load and NTSTC cases at 100%, 40%, and 20% rated load. The 100% case was included as the full-load reference, whereas the 40% and 20% cases were selected as the key low-load conditions. The 50% OMB case was retained because its corresponding air-distribution scheme was specifically used within the 47%-50% load range. Direct OMB-versus-NTSTC comparisons were conducted at the common nominal loads of 100%, 40%, and 20%, with particular emphasis on the two low-load conditions. By comparing the gas-particle coupling flow characteristics of both burners under low loads, the flow mechanisms leading to combustion instability and nozzle slagging in the OMB burner are revealed, and the operational advantages of the NTSTC burner under the same conditions are further evaluated, providing a theoretical basis for the optimized design and application of burners under deep peak shaving conditions.

According to the data in Table 4, the relationship between the swirl number and the burner structure becomes clearer. For the OMB burner, as the rated load decreases from 100% to 20%, the gas-phase swirl number (S_g) decreases from 0.07 to 0.03, and the particle-phase swirl number (S_p) decreases from 0.19 to 0.09, which is closely related to the reduction in primary air flow rate. Although the primary air of the OMB burner is a rotating flow, the weak swirling effect of the swirl channel results in an almost complete loss of rotational capability after ejection. Particularly, the high axial velocity of the primary air in the low-airflow combustion chamber leads to a low swirl number.

In contrast, the swirl numbers of the NTSTC burner are consistently higher than those of the OMB. As the rated load decreases from 100% to 20%, the gas-phase swirl number decreases from 0.30 to 0.23, and the particle-phase swirl number decreases from 0.31 to 0.27. Although the NTSTC burner eliminates the swirl channel, the introduced gap air and its guide vanes create a stable recirculation zone in the burner outlet region, enabling it to maintain high S_g and S_p values even under different unit loads. Overall, the burner structure significantly influences the swirl number. The NTSTC exhibits higher swirl numbers in these aspects, resulting in higher swirl numbers across all load conditions compared to the OMB burner.

Table 4. Gas-Particle two-phase experiment parameters.

Burner	Load	Primary air flow rate (m^3/h)	Interstitial air flow rate (m^3/h)	Total secondary air flow rate (m^3/h)	Total air flow rate (m^3/h)	S_g	S_p
OMB	100%	229.84	-	585.58	815.42	0.07	0.19
	50%	176.35	-	494.69	671.04	0.05	0.16
	40%	156.75	-	443.79	600.54	0.03	0.14
	20%	130.64	-	392.90	523.54	0.03	0.09
NTSTC	100%	229.84	44.75	630.33	860.17	0.30	0.31
	40%	156.75	34	477.79	634.54	0.29	0.31
	20%	130.64	24.25	417.15	547.79	0.23	0.27

Note: The total secondary-air flow rate of the NTSTC includes the interstitial-air flow.

4. Results and Discussion

4.1. Velocity Field

The axial velocity distribution at the outlet of OMB and NTSTC under different load conditions is shown in Figure 4. In the axial velocity distributions of NTSTC and OMB, the presence or absence of the RZ is the main difference in the flow characteristics of the two burners. A comparison of the outlet flow field characteristics of OMB and NTSTC at different loads reveals significant differences between the two in terms of flow organization and stable combustion capacity.

The axial average velocity distribution of the OMB burner is characterized by a single peak along the radial direction, and there is no stable RZ is formed under any investigated load, with only a very small negative velocity band near the central axis of the nozzle, which contributes limited to flame stabilization. Therefore, the overall flame stabilization performance of this type of burner is weak, especially under low load conditions. In contrast, NTSTC can form a clear central recirculation zone in the near-field area of the nozzle, whose axial velocities of the gas and particle phases show a bimodal distribution in the range of $x/d = 0.1$ - 0.5, with the main peak corresponding to the central rich combustion RZ and the secondary peak to the secondary air area, demonstrating the synergy of fuel and air at the outlet. As the flow moves downstream, the backflow intensity of NTSTC gradually weakens, the difference between the two peaks tends to decrease, while the overall gas-particle coupling remains good. Comprehensive analysis shows that the OMB outlet flow field lacks effective RZ, whereas the NTSTC exhibits a bimodal axial velocity distribution and forms a distinct central RZ in the near-field region. These flow characteristics promote particle residence and central accumulation under low-load conditions and represent favorable aerodynamic features for flame stabilization. However, the actual ignition and combustion performance was not directly measured in the present cold-flow experiment.

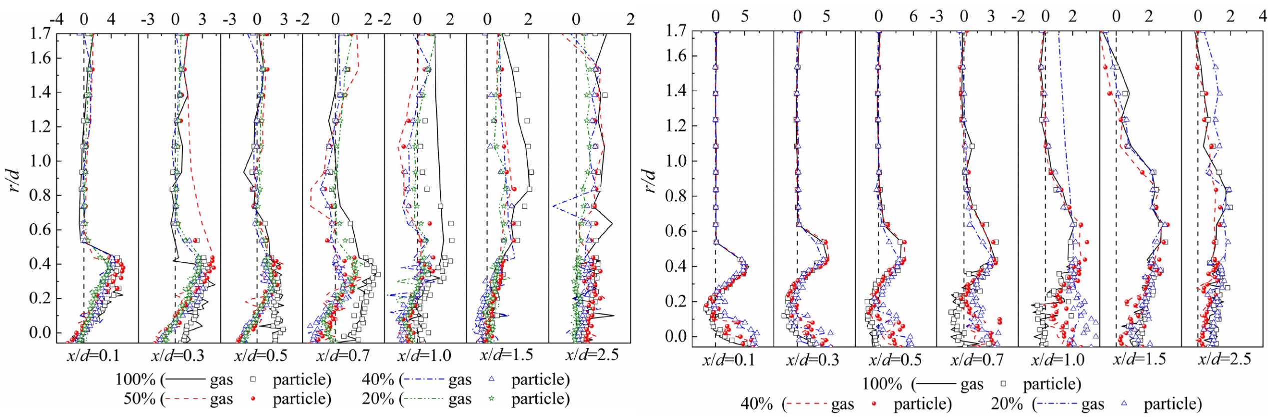

(a) OMB (b) NTSTC

Figure 4. Axial velocity distribution at the OMB and NTSTC outlet under different loads (m/s).

The radial velocity distributions of OMB and NTSTC outlets under different load conditions are shown in **Figure 5**. By comparing the radial average velocity distributions of OMB and NTSTC under different loads, the following conclusions can be drawn: the OMB outlet flow field always shows a unimodal structure, with the velocity peaks concentrated in the secondary air dominant area. With the reduction of load, only a limited attenuation occurs, and the downstream radial velocity rapidly decays to nearly zero, indicating that its radial diffusion capacity is limited and its overall stable combustion characteristics are poor. In contrast, NTSTC shows a distinct negative velocity band in the near-field region ($x/d = 0.1$ - 1.0), and the gas-particle phase shows an inward aggregation tendency in the central region, which corresponds to the axial RZ, indicating that it not only has reverse flow but also can promote the enrichment of particles in the central region, thereby significantly enhancing the heat transfer and mixing of pulverized coal with high-temperature flue gas. In the far-field region (x/d = 1.5 - 2.5), the velocity distribution of NTSTC fluctuates around 0 m/s, and the curve height is consistent under different loads, reflecting good load adaptability. Overall, OMB radial diffusion is limited and there is a lack of effective reflow, while NTSTC achieves stronger steady-burning and variable load adaptability through reflow and aggregation effects.

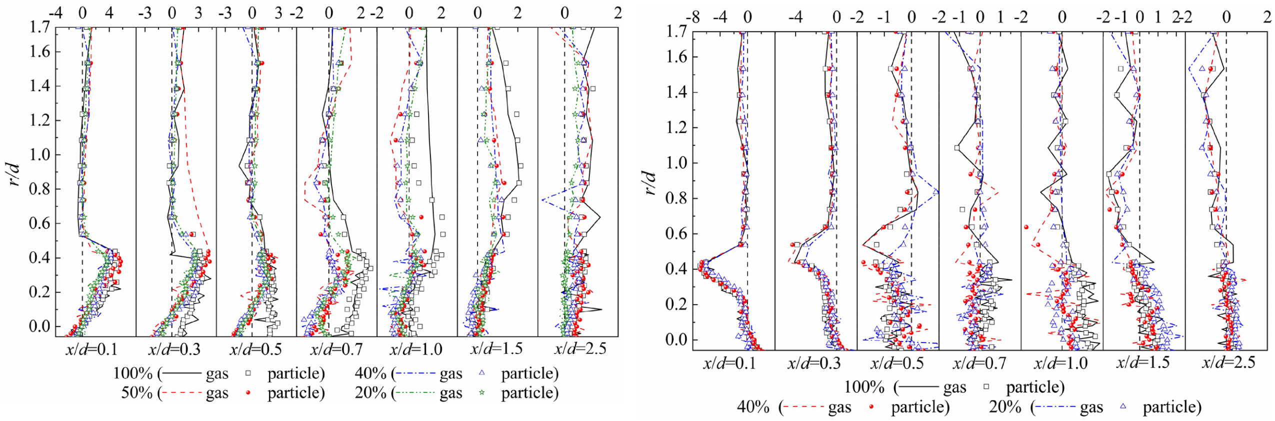

(a) OMB (b) NTSTC

Figure 5. Radial velocity distribution at the OMB and NTSTC outlet under different loads (m/s).

The tangential velocity distributions of OMB and NTSTC outlets under different load conditions are shown in **Figure 6**. A combined comparison shows that the average tangential velocity distribution of the OMB burner under different loads presents a bimodal feature, with both primary and secondary air maintaining strong rotation in the near-field region, resulting in a higher overall tangential velocity level at the outlet. However, there is local counter-swirling near the centerline, forming small-scale vortices, and this unstable flow pattern makes it more difficult for the gas-particle phase to maintain stable blending at low loads. As the load decreases, the overall tangential velocity of OMB decays significantly, and the swirl intensity is insufficient, further weakening the support for combustion stability. In contrast, the tangential velocity distribution of NTSTC has always been a single-peak structure, with peaks concentrated in the swirl secondary air zone, while the tangential velocities of the primary air and the RZ are close to zero, indicating that the flow field is dominated by axial backflow. Because the primary wind is organized in a direct current form, this structure avoids complex tangential vortices and helps to form a stable central RZ in the near field, providing conditions for pulverized coalescing, retention, and preheating. As the flow develops downstream, the tangential velocity of NTSTC gradually decays and approaches zero, but maintains a highly consistent distribution pattern under different loads, demonstrating good adaptability to various operating conditions.

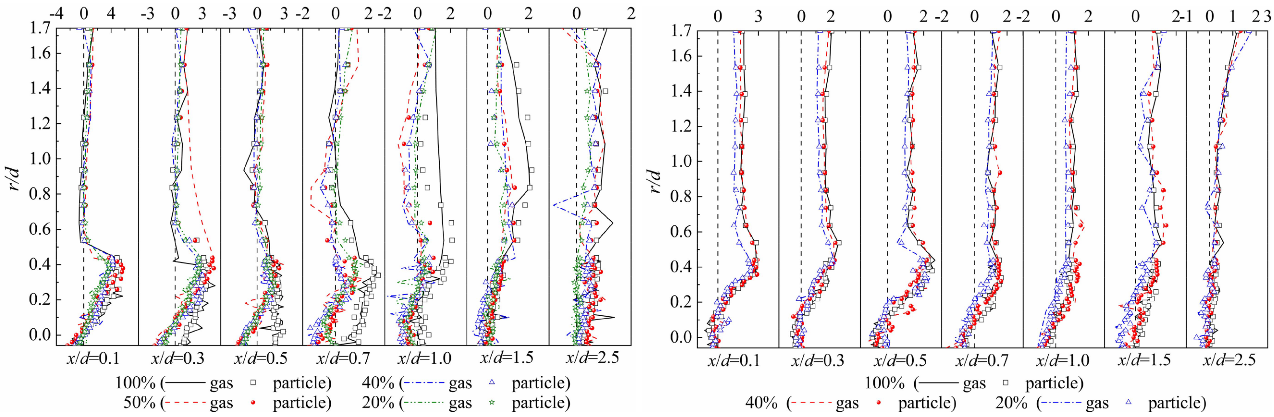

(a) OMB (b) NTSTC

Figure 6. Tangential velocity distribution at the OMB and NTSTC outlet under different loads (m/s).

4.2. RZ Boundaries

No stable gas-phase RZ is formed at the OMB outlet at any rated load, although a narrow region with slightly negative axial average velocity appears near the burner centerline. The gas-phase and particle-phase RZ boundaries at the NTSTC outlet under different rated loads are shown separately in **Figure 7**. Unless otherwise stated, the RZ length and width discussed below refer to the gas-phase RZ boundary, whereas the particle-phase RZ boundary represents the spatial range of particle recirculation. At 100% rated load, the RZ is 0.9d in length and 0.34d in width. The lower boundary of the RZ is located below the burner centerline, indicating that the RZ is the central RZ. When the rated load drops from 100% to 40%, the length of the RZ remains at 0.9d and the width is reduced to 0.24d. The position of the upper boundary of the RZ remains largely unchanged, while the lower boundary moves above the burner centerline, indicating that the recirculation zone is a longer annular recirculation zone. When the rated load drops from 40% to 20%, the length of the RZ decreases to 0.6d and the width increases to 0.32d. The length and width of the RZ are closely related to the airflow distribution in each air duct of the burner. As the rated load decreases, the volume of both the direct current primary air and the swirl secondary air decreases.

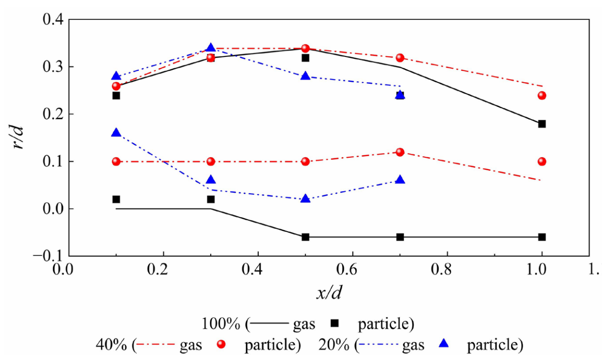

Figure 7. Gas-phase and particle-phase RZ boundaries at the NTSTC outlet under different rated loads.

The reduction in the velocity of the direct current primary air is beneficial for the swirl secondary air to draw in the primary air. At the same time, a decrease in the velocity of the swirl secondary air reduces its rotational capacity. Under the combined effect of these factors, the length and width of the RZ may show different trends of change. However, the overall range of the RZ shrinks due to a decrease in the burner swirl number. The results show that as the rated load decreases, there is a tendency for the central RZ to transform into an annular RZ, and there is a tendency for the length of the RZ to shorten. It is notable that even at 20% load, the outlet of the new stable combustion burner still has a relatively large RZ, ensuring that there is sufficient high-temperature recirculation flue gas at the burner outlet under low-load conditions, which is conducive to stable combustion of the burner under low-load conditions.

4.3. Turbulence Intensity

To evaluate the amplitude of turbulence fluctuations at the burner outlet and its influence on the stability of the flow field under different working conditions, the turbulence intensity T is calculated based on the root mean square pulsating velocity and average velocity measured by PDA. The calculation formula is [30]:

$$T = \frac{1}{U}\left(\frac{u_f^2 + v_f^2 + w_f^2}{3}\right)^{0.5} \tag{4}$$

where, u_f, v_f and w_f are axial pulsating velocity, radial pulsating velocity and tangential pulsating velocity, m/s, respectively; U represents the magnitude of the resultant three-dimensional mean velocity vector, m/s.

The turbulence intensity distribution at the OMB burner outlet under different rated loads is shown in **Figure 8(a)**. In the near-field region (x/d = 0.1 - 0.7), the radial distribution curve shows bimodal characteristics, with a smaller peak near the centerline ($r/d \approx 0$) and a higher peak in the jet boundary region (approximately $r/d \approx 0.6$). In combination with **Figure 5(a)** and **Figure 8(a)**, it can be determined that the small peak at the center line is mainly due to the local vortex area formed at the center of the primary wind, but the influence range of this vortex area is limited and basically disappears at the x/d = 1.0 section. In the mixed area of primary and secondary air, the overall level of turbulence intensity is low that results in weakened flow field pulsation, which is related to the relatively uniform mixing and gentle velocity gradient between the swirl primary and secondary air. As the jet moves downstream, the peak turbulence intensity gradually decays and basically to near zero in the far-field region (x/d = 1.5 - 2.5). It should be noted that the position of the peak turbulence intensity at the OMB outlet remains highly consistent under different loads, indicating that the flow field structure is somewhat stable under variable loads, but the overall turbulent kinetic energy level is relatively low, which is not conducive to enhancing the gas-particle two-phase blending. In contrast, the turbulence intensity distribution of the NTSTC burner is shown in **Figure 8(b)**. In the near-nozzle area, the turbulence intensity distribution of the jet is significantly uneven, showing a high level of fluctuation in the $r/d = 0$ - 0.4 range, and this area is basically consistent with the range of the RZ shown in **Figure 7**. This indicates strong velocity fluctuations and enhanced gas-particle momentum exchange within the RZ. This feature is closely related to the introduction of gap wind, which promotes the coupling of the primary and secondary air while drawing in the primary air, resulting in a significant increase in the intensity of turbulence in the near field at the outlet. As the flow developed, the peak of turbulence intensity gradually decreased, but the peak and fluctuation amplitude were basically the same under different loads in the $x/d = 0.1$ - 0.5 range, indicating that the burner could maintain a strong near-field blending capacity under different load conditions. After entering the far-field region ($x/d =$ 0.7 - 2.5), the peak turbulence intensity gradually decreases as the load decreases. Nevertheless, a relatively high turbulence level is maintained within RZ even at 20% load, indicating that the NTSTC preserves strong gas-particle mixing under low-load conditions.

The combined analysis shows that the OMB maintains a relatively low turbulence intensity over the investigated load range, whereas the NTSTC preserves stronger turbulence and gas-particle mixing through the combined effects of the RZ and interstitial air. The implications of these flow characteristics for ignition and combustion stability require further verification under reactive-flow conditions.

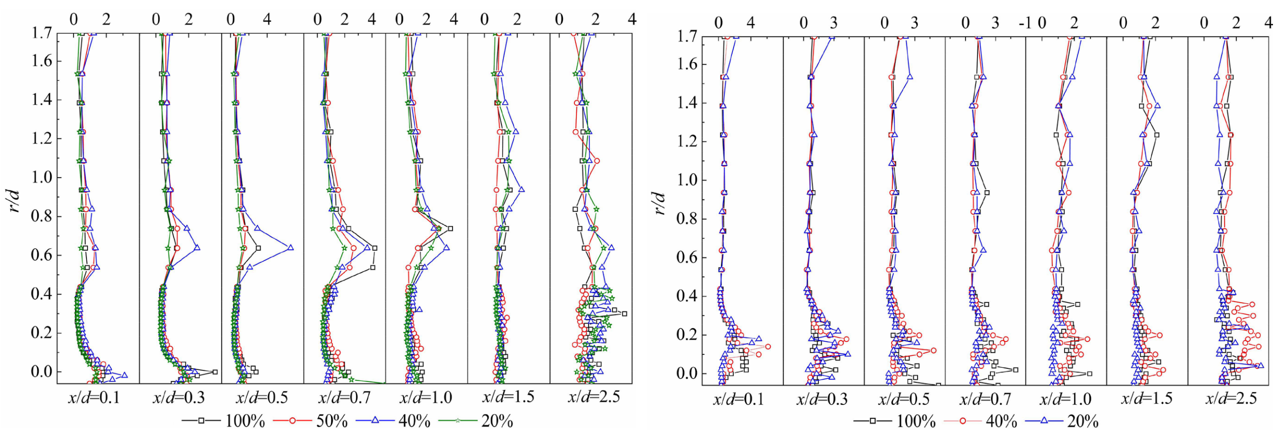

(a) OMB (b) NTSTC

Figure 8. Turbulence intensity distribution at the OMB and NTSTC outlet under different loads.

4.4. Particle Volumetric Flux Distribution

The particle volume flow distribution at the OMB burner outlet under different rated loads is shown in **Figure 9(a)**. In the near-field region ($x/d = 0.1$ - 0.7), the radial distribution curve has a single peak near $r/d = 0.3$, corresponding to the secondary air dominant zone. This is because when the primary air carries particles through the rotating device, a large number of particles are ejected along the tube wall and rapidly diffuse into the secondary air area after leaving the nozzle, resulting in a higher particle volume flow rate in this area, while the particle volume fraction near the centerline is very low. This indicates that the small-scale vortex near the nozzle center differs from a typical RZ because it has a limited spatial extent and contains very few particles. After entering the middle and far field (x/d = 1.0 - 2.5), the particles gradually gather towards the center with radial diffusion, but the overall volume flow peak shows a decreasing trend both radially and axially and the decreasing rate increases with the reduction of the rated load. This change is mainly due to the reduction in air distribution volume. Overall, the OMB maintains a relatively stable radial distribution pattern when the load is reduced, indicating that its particle transport pattern is somewhat robust.

The volume flow distribution of particles at the outlet of NTSTC under different rated loads is shown in **Figure 9(b)**. Unlike OMB, NTSTC shows a significant negative value near r/d = 0.2 in the near field (x/d = 0 - 1.0), indicating backflow of particles in this area. As shown in **Figure 7**, the negative particle volumetric flux region largely coincides with the particle-phase RZ, indicating particle backflow and accumulation within the RZ. As the rated load decreases, both the positive and negative peaks of the particle volume flow rate weaken, but the peak positions remain stable and the distribution curve shape remains almost unchanged, indicating that NTSTC can still maintain stable particle flow characteristics under load changes. In the x/d = 1.0 - 1.5 range, the particle volume flow rate increases as the load decreases, which is closely related to the reduction in the scale of the recirculation zone and the convergence of particles into the RZ. And the particle volume fraction in the area far from the nozzle decreased, further highlighting the enrichment of particles in the central area.

Overall, the particle distribution of the OMB is concentrated mainly in the secondary-air region, with a relatively low particle volumetric flux near the burner centerline. In contrast, the NTSTC produces pronounced central particle accumulation and particle backflow within the RZ. These cold-flow characteristics indicate enhanced particle residence and gas-particle interaction in the near-burner region and remain relatively stable as the load decreases.

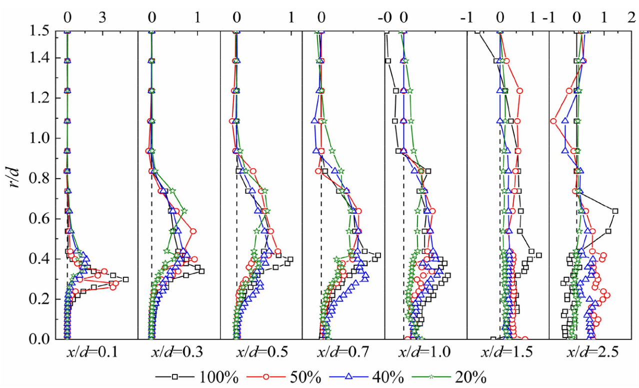

(a) OMB

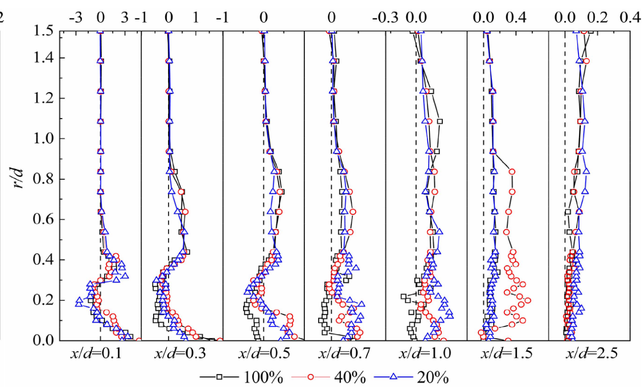

(b) NTSTC

Figure 9. Powder volume flux distribution at the OMB and NTSTC outlet under different loads. (Particle volumetric flow rate × 10^{-4} ($m^3 \cdot m^{-2} \cdot s^{-1}$)).

5. Conclusions

Based on PDA measurements, this study comparatively investigated the gas-particle two-phase flow characteristics at the outlets of the OMB and NTSTC under different nominal load conditions. The three-dimensional velocity field, turbulence intensity, RZ boundaries, and particle volumetric flux were obtained, revealing the differences in near-field flow organization between the two burners. The conclusions of this study are limited to non-reacting gas-particle flow characteristics and do not directly represent combustion efficiency, gas composition, or NO_x emissions. The main conclusions are as follows:

1) Axial and radial velocity distributions

The axial velocity at the outlet of the OMB burner shows a unimodal distribution under different loads. Only a very narrow negative-velocity region appears near the nozzle centerline, and no stable RZ is formed. The radial velocity distribution is concentrated in the secondary air area, showing only a limited attenuation as the load decreases, and the velocity in the downstream area rapidly decays to near zero. In contrast, NTSTC can form a distinct central RZ in the near-nozzle area (x/d = 0.1 - 0.5), and the axial velocity shows a bimodal distribution, with the main peak corresponding to the central RZ and the secondary peak in the secondary air area. The radial velocity is negative at $r/d \approx 0.2$, indicating the centripetal aggregation effect of the particles. These characteristics remain at low loads, indicating that the NTSTC can maintain enhanced particle residence and central accumulation over a wide range of load conditions.

2) Tangential velocity and swirl characteristics

The OMB outlet tangential velocity has a bimodal structure, with the peaks corresponding to the primary and secondary wind regions respectively, and there is counter-swirling near the centerline, forming a small-scale vortex region. As the load decreases, the rotational capacity of the burner rapidly decays, and the stability of gas-particle two-phase blending is insufficient. The tangential velocity distribution of NTSTC shows a single-peak structure, with peaks concentrated in the secondary air zone, while the tangential velocities of the primary air and the RZ are close to zero, thereby avoiding the formation of unstable vortices and keeping the near-field center recirculation stable. As the flow moves downstream, the tangential velocity gradually decays and approaches zero, and the distribution pattern is highly consistent under different loads, showing good operational adaptability.

3) Turbulence intensity and blending characteristics

The peak amplitude of the turbulence intensity of OMB is limited in the near zone of the nozzle (x/d = 0.1 - 0.7), mainly distributed in the jet boundary region where $r/d \approx 0.6$ and basically decays after $x/d = 1.0$. The overall turbulent kinetic energy level is low, which is not conducive to the enhanced mixing of particles with the airflow. The turbulence intensity of NTSTC in the near-nozzle r/d = 0 - 0.4 range is significantly enhanced and highly coincides with the central RZ, indicating that the air flow and particles are well mixed in this area. As the flow develops downstream, the turbulence intensity gradually decreases but remains relatively high within the RZ at 20% load, indicating persistent gas-particle mixing and momentum exchange under low-load conditions.

4) Particle volume distribution characteristics

The peak particle volume distribution of OMB occurs in the secondary air region ($r/d \approx 0.3$), while the concentration in the central region remains extremely low, indicating that its particle transport is mainly driven by the secondary air. As the load decreased, the attenuation of the particle volume distribution accelerated, but the overall shape remained stable. The NTSTC exhibits negative particle volumetric flux values near $r/d \approx 0.2$ in the near-field region ($x/d = 0.1$ - 1.0), reflecting particle backflow and accumulation within the RZ. This feature remains consistent across different loads, indicating that the NTSTC can maintain particle backflow and central accumulation within the RZ and exhibits better particle-flow adaptability to load variation than the OMB.

The conclusions obtained from the present cold-model experiment are primarily applicable to the intrinsic near-field gas-particle flow characteristics of an individual burner; neighboring-burner interactions and furnace-scale effects should be considered when extending these findings to the overall combustion performance of the opposed-fired boiler.

Conflicts of Interest

The author declares no conflicts of interest regarding the publication of this paper.

References

[1] Zhang, Y.Z., Wu, Q.W., Zhu, Y.F., Kang, X., Hou, B.J. and Zhou, H. (2024) Experimental Study on the Effects of Co-Firing Mode and Air Staging on the Ultra-Low Load Combustion Assisted by Water Electrolysis Gas (HHO) in a Pulverized Coal Furnace. *Journal of the Energy Institute*, **117**, Article 101828. https://doi.org/10.1016/j.joei.2024.101828

[2] Liu, T., Wang, Y.G., Zou, L., Bai, Y.Y., Shen, T., Wei, Y.W., Li, F.X. and Zhao, Q.X. (2024) Numerical Investigation of Stable Combustion at Ultra-Low Load for a 350 MW Wall Tangentially Fired Pulverized-Coal Boiler: Effect of Burner Adjustments and Methane Co-Firing. *Applied Thermal Engineering*, **246**, Article 122980. https://doi.org/10.1016/j.applthermaleng.2024.122980

[3] Wei, D.N., An, D., Wang, T., Zhang, H.C., Guo, Y.H. and Sun, B.M. (2023) Influence of Fuel Distribution on Co-Combustion of Sludge and Coal in a 660 MW Tangentially Fired Boiler. *Applied Thermal Engineering*, **227**, Article 120344. https://doi.org/10.1016/j.applthermaleng.2023.120344

[4] Huang, C.C., Li, Z.Q., Lu, Y., Chen, Z.C., Liu, H.C., Kang, Y.Y. and Wu, W. (2024) Research on a Novel Universal Low-Load Stable Combustion Technology. *Energy*, **310**, Article 133223. https://doi.org/10.1016/j.energy.2024.133223

[5] Wang, Q.X., Chen, Z.C., Li, L.K., Zeng, L.Y. and Li, Z.Q. (2020) Achievement in Ultra-Low-Load Combustion Stability for an Anthracite- and Down-Fired Boiler after Applying Novel Swirl Burners: From Laboratory Experiments to Industrial Applications. *Energy*, **192**, Article 116623. https://doi.org/10.1016/j.energy.2019.116623

[6] Zhang, H.L., Lin, H., Zhou, X., Wang, X.B., Zheng, H.G., Liu, Y. and Tan, H.Z. (2024)

CFD Modeling and Industry Application of a Self-Preheating Pulverized Coal Burner of High Coal Concentration and Enhanced Combustion Stability under Ultra-Low Load. *Applied Thermal Engineering*, **253**, Article 123831. https://doi.org/10.1016/j.applthermaleng.2024.123831

[7] Jin, W., Si, F.Q., Kheirkhah, S., Yu, C., Li, H.Y. and Wang, Y.O. (2023) Numerical Study on the Effects of Primary Air Ratio on Ultra-Low-Load Combustion Characteristics of a 1050 MW Coal-Fired Boiler Considering High-Temperature Corrosion. *Applied Thermal Engineering*, **221**, Article 119811. https://doi.org/10.1016/j.applthermaleng.2022.119811

[8] Li, Z.Q., Liu, Z., Huang, H.L., Du, H. and Chen, Z.C. (2024) The Effects of Key Parameters on the Gas/Particle Flows Characteristics in the Furnace of a Foster Wheeler Down-Fired Boiler Retrofitted with Novel Low-Load Stable Combustion Technology. *Energy*, **288**, Article 129736. https://doi.org/10.1016/j.energy.2023.129736

[9] Wang, Z.Z., Zhang, L., Zhao, Y.Y., Feng, S., Ma, J., Kong, W.W., Shen, B.X. and Sun, R. (2021) Experimental Investigation on the Evolution Characteristics of Anthracite-N and Semi-Coke Reactivity under Various O_2/H_2O Pre-Oxidation Atmospheres. *Fuel Processing Technology*, **216**, Article 106725. https://doi.org/10.1016/j.fuproc.2021.106725

[10] Wang, Y.Q., Zhou Y.G., Bai, N.M. and Han, J.C. (2020) Experimental Investigation of the Characteristics of Nox Emissions with Multiple Deep Air-Staged Combustion of Lean Coal. *Fuel*, **280**, Article 118416. https://doi.org/10.1016/j.fuel.2020.118416

[11] Hui, J.C., Zhu, S.J., Li, Z.Y., Lin, J.G., Cao, X.Y. and Lyu, Q.G. (2024) Experimental Study on Peak Shaving during Preheating Combustion for Different Coal Ranks: Thermal Modification and Variable Load Operation. *Fuel*, **373**, Article 132324. https://doi.org/10.1016/j.fuel.2024.132324

[12] Ma, D.F., Zhang, S.Y., He, X., Ding, X., Li, W.F. and Liu, P.Y. (2024) Combustion Stability and NO Emission Characteristics of Three Combustion Modes of Pulverized Coal Boilers under Low or Ultra-Low Loads. *Applied Energy*, **353**, Article 121998. https://doi.org/10.1016/j.apenergy.2023.121998

[13] Yuan, Z.H., Chen, Z.C., Wu, X.L., Zhang, N., Bian, L.G., Qiao, Y.Y., Li, J.W. and Li, Z.Q. (2022) An Innovative Low-Nox Combustion Technology for Industrial Pulverized Coal Boiler: Gas-Particle Flow Characteristics with Different Radial-Air-Staged Levels. *Energy*, **260**, Article 125142. https://doi.org/10.1016/j.energy.2022.125142

[14] Zhao, L.L., Zhou, Q.T. and Zhao, C.S. (2008) Flame Characteristics in a Novel Petal Swirl Burner. *Combustion and Flame*, **155**, 277-288. https://doi.org/10.1016/j.combustflame.2008.04.012

[15] Yan, R., Chen, Z.C., Zheng, Y., Yuan, L.X., Zeng, L.Y. and Li, Z.Q. (2021) Influence of Inner and Outer Secondary Air Ratio on Flow and Combustion Characteristics of a Swirl Burner in a 29 MW Pulverized Coal Boiler. *Energy*, **237**, Article 121625. https://doi.org/10.1016/j.energy.2021.121625

[16] Su, X.Q., Fang, Q.Y., Ma, L., Yao, B., Li, Y., Zhao, X.P., Mao, R. and Yin, C.G. (2023) Improving Combustion and Lowering NO Emissions of an Industrial Coal Swirl Burner by Optimizing Its Nozzle Structure. *Applied Thermal Engineering*, **218**, Article 119340. https://doi.org/10.1016/j.applthermaleng.2022.119340

[17] Song, M.H., Huang, Q., Niu, F. and Li, S.Q. (2020) Recirculating Structures and Combustion Characteristics in a Reverse-Jet Swirl Pulverized Coal Burner. *Fuel*, **270**, Article 117456. https://doi.org/10.1016/j.fuel.2020.117456

[18] Ti, S.G., Chen, Z.C., Li, Z.Q., Zhang, X.Q., Zhang, H., Zou, G.P., Zeng, L.Y. and Zhu, Q.Y. (2015) Effects of the Outer Secondary Air Cone Length on the Combustion

Characteristics and NO X Emissions of the Swirl Burner in a 0.5 MW Pilot-Scale Facility during Air-Staged Combustion. *Applied Thermal Engineering*, **86**, 318-325. https://doi.org/10.1016/j.applthermaleng.2015.04.021

[19] Su, X.Q., Jiang, J.L., Ma, C.L., He, Y.C. and Yang, Z.F. (2025) High-Efficiency Combustion and Low-Nitrogen Emission of Coal-Fired Boiler Based on Synergistic Optimization of Swirl Burner Structure and Air-Staged Technology. *Fuel*, **388**, Article 134352. https://doi.org/10.1016/j.fuel.2025.134352

[20] Huang, C.C., Li, Z.Q., Wang, Y.F., Fang, F., Liu, H.C., Chen, Z.C. and Liu, Y.J. (2024) Influence of Secondary Air Blade Angle and Oxygen-Rich Combustion Characteristics of an Improved Babcock Swirl Burner. *Applied Thermal Engineering*, **241**, Article 122383. https://doi.org/10.1016/j.applthermaleng.2024.122383

[21] Wang, Y.Q. and Zhou, Y.G. (2020) Numerical Optimization of the Influence of Multiple Deep Air-Staged Combustion on the Nox Emission in an Opposed Firing Utility Boiler Using Lean Coal. *Fuel*, **269**, Article 116996. https://doi.org/10.1016/j.fuel.2019.116996

[22] Lee, B.H., Song, J.H. and Kim, R.G. (2010) Simulation of the Influence of the Coal Volatile Matter Content on Fuel NO Emissions in a Drop-Tube Furnace. *Energy & Fuels*, **24**, 4333-4340. https://doi.org/10.1021/ef1003792

[23] Song, W.H., Ouyang, Z.Q., Wang, M.H., Li, S.Y., Liu, J.Z., Yu, Q., Liu, W. and Zhu, Q.Y. (2020) The Combustion and Nox Emission Characteristics of the Ultra-Low Volatile Fuel Using the Novel Pulverized Coal Self-Sustained Preheating Combustion Technology. *Fuel*, **271**, Article 117592. https://doi.org/10.1016/j.fuel.2020.117592

[24] Wang, Q.X., Chen, Z.C., Chen, Q.W., Zeng, L.Y. and Li, Z.Q. (2019) Experimental Investigation of Gas/Particle Two-Phase Flow Characteristics in a Down-Fired Boiler by PDA Measurements. *Experimental Thermal and Fluid Science*, **107**, 38-53. https://doi.org/10.1016/j.expthermflusci.2019.05.014

[25] Wang, Q.X., Chen, Z.C., Han, H., Tu, Y.J., Liu, G.K., Zeng, L.Y. and Li, Z.Q. (2019) Detailed Gas/Particle Flow Characteristics of an Improved Down-Fired Boiler with Respect to a Critical Factor Affecting Coal Burnout: Vent-Air Inclination Angle. *Energy*, **182**, 570-584. https://doi.org/10.1016/j.energy.2019.06.057

[26] Pickett, L.M., Jackson, R.E. and Tree, D.R. (1999) LDA Measurements in a Pulverized Coal Flame at Three Swirl Ratios. *Combustion Science and Technology*, **143**, 79-107. https://doi.org/10.1080/00102209908924194

[27] Zhang, X., Chen, Z.C., Hou, J., Liu, Z., Zeng, L.Y. and Li, Z.Q. (2022) Evaluation of Wide-Range Coal Combustion Performance of a Novel Down-Fired Combustion Technology Based on Gas-Solid Two-Phase Flow Characteristics. *Energy*, **248**, Article 123662. https://doi.org/10.1016/j.energy.2022.123662

[28] Ren, F., Li, Z.Q., Chen, Z.C., Xu, Z.X. and Yang, G.H. (2010) Experimental Investigations into Gas/Particle Flows in a Down-Fired Boiler: Influence of the Vent Air Ratio. *Energy & Fuels*, **24**, 1592-1602. https://doi.org/10.1021/ef901243c

[29] Lira, S.H., Torres, M.J., Guerra, S.R. and Zahr, V.J. (2021) Numerical Characterization of the Solid Particle Accumulation in a Turbulent Flow through Curved Pipes by Means of Stokes Numbers. *Applied Sciences*, **11**, Article 7381. https://doi.org/10.3390/app11167381

[30] Fan, W.D., Lin, Z.C., Li, Y.Y. and Li, Y. (2010) Effect of Temperature on NO Release during the Combustion of Coals with Different Ranks. *Energy & Fuels*, **24**, 1573-1583. https://doi.org/10.1021/ef901198j